The Astrophysical Journal, 697:1918–1927, 2009 June 1 doi:10.1088/0004-637X/697/2/1918

ROTATION OF CORONAL MASS EJECTIONS DURING ERUPTION

B. J. Lynch[1], S. K. Antiochos[2], Y. Li[1], J. G. Luhmann[1], and C. R. DeVore[3]
[1] Space Sciences Laboratory, University of California, Berkeley, CA, USA; blynch@ssl.berkeley.edu; yanli@ssl.berkeley.edu; jgluhman@ssl.berkeley.edu
[2] NASA Goddard Space Flight Center, Greenbelt, MD, USA; spiro.k.antiochos@nasa.gov
[3] Laboratory for Computational Physics and Fluid Dynamics, Naval Research Laboratory, Washington, DC, USA; devore@lcp.nrl.navy.mil
Received 2008 November 29; accepted 2009 March 26; published 2009 May 15

ABSTRACT

Understanding the connection between coronal mass ejections (CMEs) and their interplanetary counterparts (ICMEs) is one of the most important problems in solar-terrestrial physics. We calculate the rotation of erupting field structures predicted by numerical simulations of CME initiation via the magnetic breakout model. In this model, the initial potential magnetic field has a multipolar topology and the system is driven by imposing a shear flow at the photospheric boundary. Our results yield insight on how to connect solar observations of the orientation of the filament or polarity inversion line (PIL) in the CME source region, the orientation of the CME axis as inferred from coronagraph images, and the ICME flux rope orientation obtained from in situ measurements. We present the results of two numerical simulations that differ only in the direction of the applied shearing motions (i.e., the handedness of the sheared-arcade systems and their resulting CME fields). In both simulations, eruptive flare reconnection occurs underneath the rapidly expanding sheared fields transforming the ejecta fields into three-dimensional flux rope structures. As the erupting flux ropes propagate through the low corona (from 2 to 4 $R_\odot$) the right-handed breakout flux rope rotates clockwise and the left-handed breakout flux rope rotates counterclockwise, in agreement with recent observations of the rotation of erupting filaments. We find that by 3.5 $R_\odot$ the average rotation angle between the flux rope axes and the active region PIL is approximately 50°. We discuss the implications of these results for predicting, from the observed chirality of the pre-eruption filament and/or other properties of the CME source region, the direction and amount of rotation that magnetic flux rope structures will experience during eruption. We also discuss the implications of our results for CME initiation models.

Key words: Sun: corona – Sun: coronal mass ejections (CMEs) – Sun: magnetic fields

1. INTRODUCTION

Coronal mass ejections (CMEs) and their interplanetary manifestations (ICMEs) are some of the most dramatic and important examples of large-scale transient energy release by the dynamic Sun. Many CMEs appear to have a coherent, ordered, large-scale magnetic structure that can be well approximated by a magnetic flux rope. The traditional three-part white light structure seen in coronagraph observations (e.g., Illing & Hundhausen 1986; Hundhausen 1999) has been interpreted as being consistent with viewing a magnetic flux rope structure (Dere et al. 1999; Plunkett et al. 2000; Cremades & Bothmer 2004; Thernisien et al. 2006). The most well-structured ICMEs are now called magnetic clouds (MCs), typically defined through in situ observations of extended periods of enhanced field magnitude, smooth field rotation, and low proton temperature or plasma beta (Klein & Burlaga 1982; Lepping et al. 1990; Gosling et al. 1973; Richardson & Cane 1995), and these properties are often coincident with counterstreaming electron (Zwickl et al. 1983; Gosling et al. 1987) and/or enhanced elemental and ionic compositional signatures (e.g., Borrini et al. 1982; Galvin 1997; Zurbuchen & Richardson 2006, and references therein). For several decades now, various flux rope models have been used to explain the observed magnetic field signatures within MCs (Goldstein 1983; Marabushi 1986; Burlaga 1988; Lepping et al. 1990; Vandas et al. 1993; Mulligan & Russell 2001; Hildago et al. 2002). These studies typically derive an axial orientation for the cylindrical and elliptical models (e.g., Lepping et al. 1990; Mulligan & Russell 2001) or a plane of symmetry for the two-dimensional reconstruction models (Hu & Sonnerup 2001). In this paper, we focus on the near-Sun CME dynamics that produce a large-scale rotation of the entire magnetic flux rope structure, i.e., the time evolution of the overall orientation of the coherent CME fields or, equivalently, the axial/plane-of-symmetry orientation of the various flux rope model approximations.

MC ICMEs are some of the most geoeffective solar wind structures because they are often associated with enhanced southward field components, either directly as part of the internal magnetic structure of the flux rope, or in the surrounding sheath region due to the compression of the upstream ambient solar wind field and density (e.g., Tsurutani et al. 1988; Zhang et al. 2004; Huttunen et al. 2005, and references therein). Thus, from a space weather prediction standpoint, the ability to forecast this southward component (B_z in GSE coordinates) of CME/ICME field structure for Earthward-directed CMEs is greatly desired. The magnetic orientation of these structured flux rope CME/ICMEs can be either directly observed or indirectly inferred at several different points during their evolution: starting from their initiation in the low solar atmosphere, through their propagation through the extended corona, and finally to their in situ measurement by a spacecraft in the heliosphere.

The magnetic configuration of the CME source region prior to eruption is believed to yield constraints on the magnetic orientation of the subsequent erupting structure. In some cases, line of sight and vector magnetograms, observations of filament material, and calculated source region helicities can be used to estimate the MC orientation and handedness (e.g., Bothmer & Schwenn 1998; Zhao & Hoeksema 1998; Yurchyshyn et al. 2001, and references therein) with the reasonable assumption that the highly sheared fields parallel to the local PIL correspond to the axis of the flux rope and the overlying surrounding fields become the azimuthal or twist component. However, while essentially all CMEs originate from stressed magnetic fields

associated with PILs, only ∼30%–50% of ICMEs have enough observed internal structure to be considered MCs (Gosling 1990; Cane et al. 1997). In addition to the CME source region, the orientation of the coronal helmet streamer belt is likely to have significant influence over the eventual orientation of the MC (Crooker et al. 1993; Zhao & Hoeksema 1996; Mulligan et al. 1998; Yurchyshyn 2008).

A technique for estimating the CME/ICME large-scale magnetic flux rope orientation from white light coronagraph observations of halo CMEs has been recently developed. By fitting a parameterized flux rope (with an associated density model) to halo CME observations, it has been demonstrated that the elliptical elongation of the halo CME structure is a fairly accurate proxy for the axial orientation of the model flux rope structure (Thernisien et al. 2006; Krall et al. 2006; Yurchyshyn et al. 2007). Recent work has also shown that there exists a good correlation between the directly and indirectly observed CME–ICME/MC orientation, defined in terms of a flux rope topology, throughout the various stages of CME eruption and propagation into the heliosphere. Yurchyshyn et al. (2007) find that for a majority (∼64%) of their 25 well-established CME–MC pairs, the MC axis orientation is within ±45° of the major axis of the ellipse used to fit the haloCME event in coronagraph observations. Additionally, the ellipse orientations correlate equally well, albeit within the same uncertainty, with the inferred orientation from various solar source indicators (Yurchyshyn 2008).

We propose that the origin of this ±45° uncertainty in the analyses thus far of the various measures and correlations of pre-eruption orientation, coronagraph orientation, and interplanetary flux rope orientation is due, at least in part, to the dynamics of the eruption process itself. In particular, there is likely to occur a large-scale rotation of the entire flux rope structure during the initial phases of the eruption.

There is substantial observational and theoretical evidence for such CME flux rope rotation. Green et al. (2007) have examined a number of filament eruptions associated with transient sigmoid features and characterized their rotation during eruption. They review a number of models for sigmoid formation and associated CME eruptions and find that both sheared-arcade models and flux rope models agree with the observed relationship between positive (negative) helicity and clockwise (counterclockwise) rotation. These authors describe this observed property simply as a consequence of helicity conservation, where, for a magnetic flux rope, the relative helicity can be written as $H_r = \Phi^2(T+W)$, where T is the twist per unit length and W is the writhe of the flux rope axis. The apparent "unraveling" of filament material implies a decrease of twist, which under conservation of the magnetic flux and helicity (i.e., ideal magnetohydrodynamics (MHD)) must be converted into an increase of writhe.

Similar rotation is also seen in numerical simulations of erupting flux ropes (Fan & Gibson 2004; Török et al. 2004). In this paper, we present the first demonstration of this property for three-dimensional sheared-arcade fields that are transformed into erupting flux rope structures through the eruptive flare reconnection process. Green et al. (2007) discuss the tether-cutting model (Moore et al. 2001) as their representative sheared-arcade example, which is applicable to our simulations as well: the magnetic breakout model for CME initiation provides a self-consistent invocation of tether-cutting reconnection (i.e., the eruptive flare reconnection) as a consequence of the runaway breakout reconnection and associated expansion (e.g., Antiochos et al. 1999; MacNeice et al. 2004; Lynch et al. 2008). Green et al. state that while their observational results are in full agreement with both the flux rope models and the tether-cutting sheared-arcade model, they prefer the former given their interpretation of pre-eruption topology of filament/prominence field structure. Proponents of the sheared-arcade models for prominence structure argue that high-resolution and high-cadence observations of prominence material imply an overall ribbon-like topology composed of many filamentary strands (e.g., Martin 1998; Lin et al. 2008), and that the apparent helical structure in some quiescent prominences can be explained as an illusion caused by the counterstreaming of material on field lines that cross along the line of sight (Panasenco & Martin 2008). Our purpose here however is not to settle the debate on filament field geometry. Rather, we will focus on understanding the relationship between the source region, CME and ICME magnetic structure, and its dynamic evolution.

The structure of the paper is as follows. In Section 2, we briefly describe the MHD code and the initial conditions for the right-handed (RH) and left-handed (LH) breakout numerical simulations. In Section 3, we present the results showing that our breakout flux ropes undergo a significant rotation, up to ∼50° ± 20°, as they erupt through ∼2 $R_\odot$ of the closed field corona and that the direction of their rotation obeys the expected helicity- or handedness-rotation relationship, i.e., the RH flux rope rotates clockwise and the LH flux rope rotates counterclockwise. We also discuss the physical mechanisms responsible for this rotation and argue that it is fundamentally due to the "sigmoidality" of the pre-flare field configuration and the balance of internal and external forces during the eruption process rather than the onset of an MHD kink instability. In Section 4, we summarize the simulation results and our conclusions.

2. THE MHD MODEL

The numerical simulations are performed with the Adaptively Refined MHD Solver (ARMS) code developed at the Naval Research Laboratory. ARMS solves the ideal MHD equations in native spherical coordinates utilizing flux-corrected transport schemes (DeVore 1991). ARMS uses the PARAMESH package for the block-adaptive gridding and multiprocessor parallelization (MacNeice et al. 2000). The computational domain covers $1 \leqslant r \leqslant 20\ R_\odot, 0.0625\pi \leqslant \theta \leqslant 0.9375\pi$, and $-0.5\pi \leqslant \phi \leqslant 0.5\pi$. The coarsest grid resolution in (r, θ, ϕ) is $40 \times 40 \times 40$, with three additional levels of grid refinement that each double the resolution for a total of ∼3.5 million computational cells.

Initial magnetic field. The initial magnetic field for both the right- and left-handed simulations is shown in the left panel of Figure 1. This initial field configuration is given by the superposition of six magnetic dipole sources, one at the origin to create the background field, and the other five near to the surface to create the strong bipolar region. These five dipoles are aligned so that the two polarity spots they create at the surface are extended in longitude (Figure 1). The specific dipole parameters and a detailed analysis of the CME initiation and eruption properties for the RH eruption will be described in a forthcoming publication (B. J. Lynch et al. 2009, in preparation).

Initial solar atmosphere. The solar atmosphere density, pressure, and temperature profiles are given in Lynch et al. (2008; Section 3.2.2) and the resulting plasma β and Alfven speed profiles are qualitatively similar. The plasma is polytropic with $\gamma = 5/3$ and does not include any additional coronal heating. Consequently, there is no solar wind outflow and the magnetic

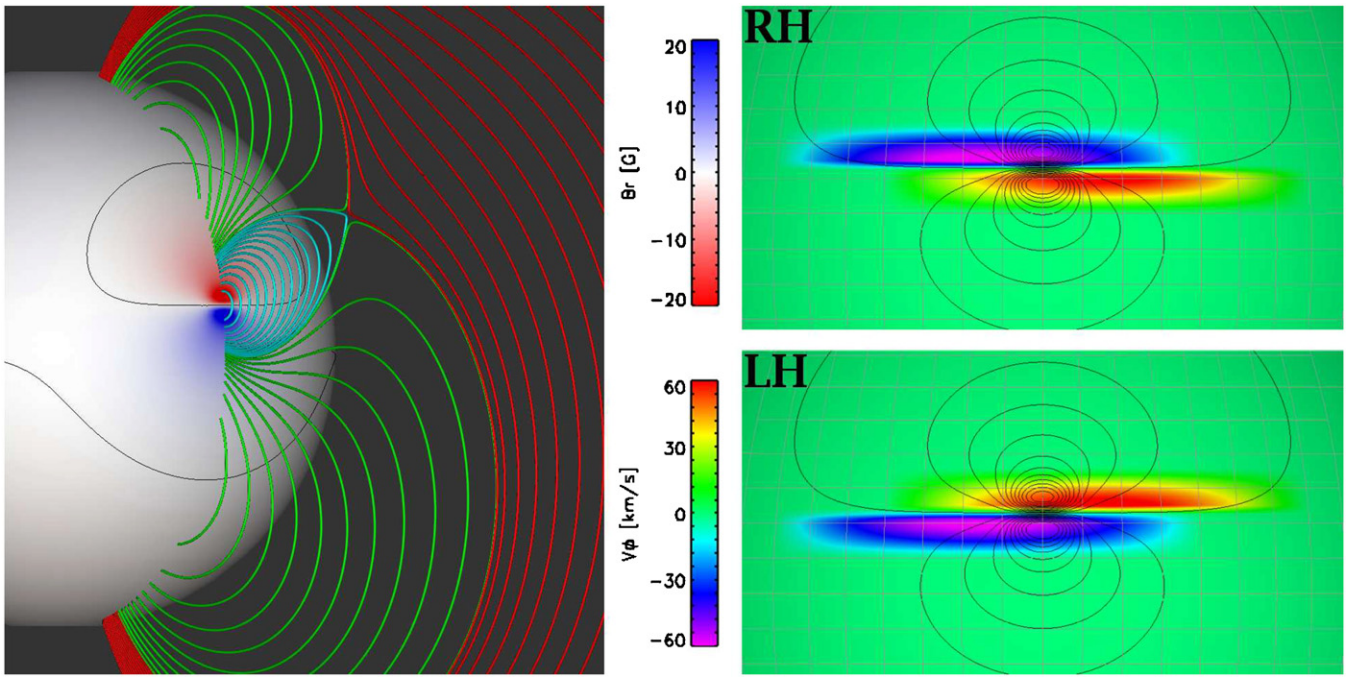

Figure 1. Left panel shows the initial potential field configuration for our multipolar magnetic breakout simulations with a three-dimensional coronal null point above the active region polarity inversion line. The right panel plots the RH (top) and LH (bottom) shearing flows v_ϕ at their maximum value ($t = 5000$ s) over contours of the initial B_r. The grid lines indicate the computational block boundaries.

fields are closed throughout the entire computational domain. Therefore, our simulations model the dynamics of breakout CME initiation and propagation through the closed field corona, such as within the coronal helmet streamer belt.

Imposed shearing flows. The shearing flows for each simulation are shown in the right panel of Figure 1. In the RH case (top), the negative spot is sheared to the left and the positive spot is sheared to the right, and vice versa for the LH case (bottom). The flows for each simulation are given by $\boldsymbol{v} = (v_1 + v_2)\hat{\boldsymbol{\phi}}$, where in each case, v_1 and v_2 represent the flow patterns north and south of the active region PIL, respectively. They are given as

$$v_1 \sim \sin\left[\pi(\theta - 0.423)/(0.10)\right] \sin\left[\pi\phi_1^{\mathrm{R,L}}/0.55\right] \quad (1)$$

$$v_2 \sim \cos\left[\pi(\theta - 0.452)/(0.10)\right] \sin\left[\pi\phi_2^{\mathrm{R,L}}/0.55\right], \quad (2)$$

with $\phi_1^{\mathrm{R}} = \phi_2^{\mathrm{L}} = \phi - 0.0375$ and $\phi_2^{\mathrm{R}} = \phi_1^{\mathrm{L}} = \phi + 0.0375$. The θ-spatial extent of the shear flows in both simulations is defined as v_1 vanishes outside: $0.423\pi \leqslant \theta \leqslant 0.448\pi$ and v_2 vanishes outside: $0.452\pi \leqslant \theta \leqslant 0.477\pi$. The ϕ-spatial extent for the RH shearing flows is defined as v_1 vanishes outside $-0.1\pi \leqslant \phi \leqslant 0.175\pi$ and v_2 vanishes outside $-0.175\pi \leqslant \phi \leqslant 0.1\pi$, and for the LH shearing flows, v_1 vanishes outside $-0.175\pi \leqslant \phi \leqslant 0.1\pi$ and v_2 vanishes outside $-0.1\pi \leqslant \phi \leqslant 0.175\pi$. All the shearing profiles have a $1 - \cos(2\pi t/10^4)$ temporal dependence, so that they reach a maximum value of ± 65 km s^{-1} at $t = 5000$ s. The flows are set to zero for $t \geqslant 10^4$ s.

Our applied shearing flows, while necessarily simpler than real photospheric flows observed on the Sun (Li et al. 2004), are a reasonable approximation for the generation of a significant magnetic field component parallel to the local PIL. Observations of flux emergence often show a strong shear component (e.g., Strous et al. 1996) and this property has been reproduced in numerical simulations of flux emergence (e.g., Manchester 2001; Magara & Longcope 2003). Manchester (2003) showed that these shearing flows could destabilize the emerging field, describing a self-consistent relationship between the mechanism of free magnetic energy generation and CME initiation, and these shear flow magnitudes have been favorably compared to coronal velocities obtained by spectroscopic doppler shifts (Manchester 2008; Chae et al. 2000). Additionally, observations and simulations of magnetic flux evolution on longer timescales show that the cumulative effects of differential rotation and meridional flow can also build up a similar sheared field component (van Ballegooijen et al. 1998; Sheeley 2005).

Boundary onditions. The boundary conditions at both the inner and outer radial boundaries are line-tied and no-flow-through $v_r = 0$. Consequently, the field line footpoints are fixed at the boundaries, except in the region of imposed shear flows. These boundary conditions imply that any eruption will eventually be stopped by the upper boundary, but we terminate the simulations well before then. In all of our results presented below, the CME height is $\leqslant 5\ R_\odot$.

3. SIMULATION RESULTS

3.1. Eruption-Induced Rotation

Figure 2 shows the evolution of the normal magnetic field B_r at the bottom boundary due to the applied shearing and the resulting coronal field structures. The left and right panels of Figure 2 present the results for the LH and RH simulations, respectively, corresponding to the field structure at $t = 9000$ s prior to the onset of the eruptive flare reconnection. Although not visible from this perspective, the overlying breakout reconnection is well underway by this time resulting in the increasing radial expansion of the sheared fields. Note that the LH and RH strongly sheared core field has an inverse-S and S-sigmoidal geometry, in agreement with observations. The two chiralities represent the observed sense of sigmoids and their active region fields in opposite hemispheres (e.g., Canfield et al. 2007; Pevtsov et al.

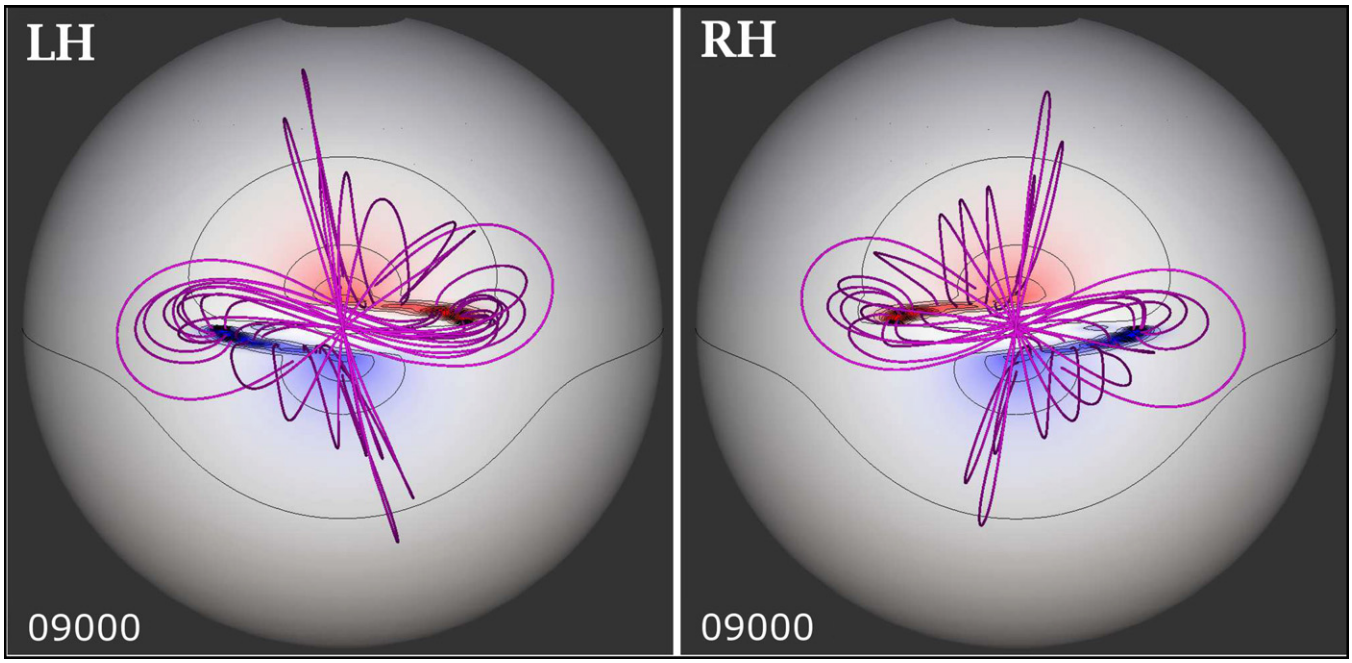

Figure 2. Representative field lines showing the sheared field configuration at $t = 9{,}000$ s prior to the eruptive flare reconnection for the LH (left-column) and RH (right-column) simulations. The B_r flux distribution on the inner boundary is shown in the same colorscale as Figure 1. Note the LH, RH sheared fields naturally form inverse-S and S-shaped sigmoids, respectively.

1995) or in the same hemisphere during consecutive phases of the solar cycle (e.g., Bothmer & Schwenn 1998). Our final flux distribution, and therefore the sigmoidal field structure, is obviously much larger than is observed on the real Sun. Our simulation's final active region area is approximately 10–30 times larger in each spatial dimension than is typically observed in active regions associated with eruptive sigmoids (Canfield et al. 1999). However, the relative length-to-width proportion of our shear channel (∼5:1), and therefore the overall skew or "sigmoidality" of our pre-eruption structure, matches the observed length-to-width ratio of soft X-ray sigmoids quite well (e.g., Rust & Kumar 1996).

The eruptive flare reconnection starts at approximately $t = 10{,}000$ s in these simulations. From this point onward, the erupting fields take on a flux rope structure due to the flare reconnection's addition of a highly twisted component that surrounds the original sheared field core. The time evolution of the LH eruption and its counterclockwise rotation is plotted in Figure 3. The left column shows the erupting flux rope structure and representative field lines from a head-on view, comparable to the view of an Earth-directed halo CME. The representative axial field lines are plotted in green and the surrounding flux rope poloidal field lines are plotted in magenta. The evolution of the angle between the section of the green axial field lines that pass through the center of the erupting flux rope structure and the original source region PIL is quite clear. At $t = 10{,}000$ s the axial field lines are roughly parallel to the source region PIL, yet by $t = 13{,}000$ s the axial field lines are highly inclined. The right column of Figure 3 plots the same axial (green) and twisted (magenta) field lines from an edge-on view, roughly analogous to a limb-CME view. In addition, field lines from the surrounding flux systems participating in the breakout CME eruption are plotted in dark blue. The classic flux rope structure is easily recognizable from this perspective, as is the evolving orientation of the flux rope axis, from perpendicular to the plane of the sky to having a significant component projected into it.

To determine a quantitative measure of the rotation angle and its time evolution we create field line plots in the style of the left column of Figure 3 and overplot a pair of axes $(\hat{\boldsymbol{n}}, \hat{\boldsymbol{m}})$ corresponding to the angle α of the representative axial field lines. An illustrative example is shown in Figure 4 with the original (blue) and rotated (black) axes plotted over the RH eruption at $t = 12{,}000$ s. For this time slice, the average rotation angle is determined to be $\alpha = 35°$. The $n-$axis approximates the major axis of the ellipse defined by the projected extent of the magenta field lines onto the plane of the sky (i.e., the plane of our image). The line perpendicular to the angle of the axial field lines, the $m-$axis, is also the minor axis of the projected ellipse and corresponds to the angle that the highly twisted field lines of the flux rope boundary have rotated out of the $\phi = 0$ plane.

Since the flux rope is a continuous structure, the selection of the axial (green) field lines has a significant uncertainty associated with it. To compensate, we select a range of field lines (typically between 4 and 8) spaced at radial intervals of 0.05 $R_\odot$ through the center of the erupting structure. This yields a typical spread in the rotation angle of $\pm 10°$–$20°$ for each of the time slices. The time slices are taken every 500 s starting at the onset of the flare reconnection $t = 10{,}000$ s through 13,000 s when the center of the erupting flux rope has reached ∼3.5 $R_\odot$.

The rotation angles that we obtain from the procedure described above are plotted in Figure 5. The red points are from the RH simulation and show the time evolution of the average apparent clockwise rotation of the flux rope axis as it propagates through the low corona. The blue points plot the counterclockwise rotation of the LH simulation. The X-axis error bars denote the radial range of the axial field lines used to estimate the flux rope rotation angle. Both eruptions show an average rotation rate of approximately $30°\ R_\odot^{-1}$, or equivalently in these simulations, approximately $1°\ \mathrm{min}^{-1}$, due to our moderate eruption speed of ∼400 km s^{-1}. The overall rotation of the erupting flux rope can also be readily seen in

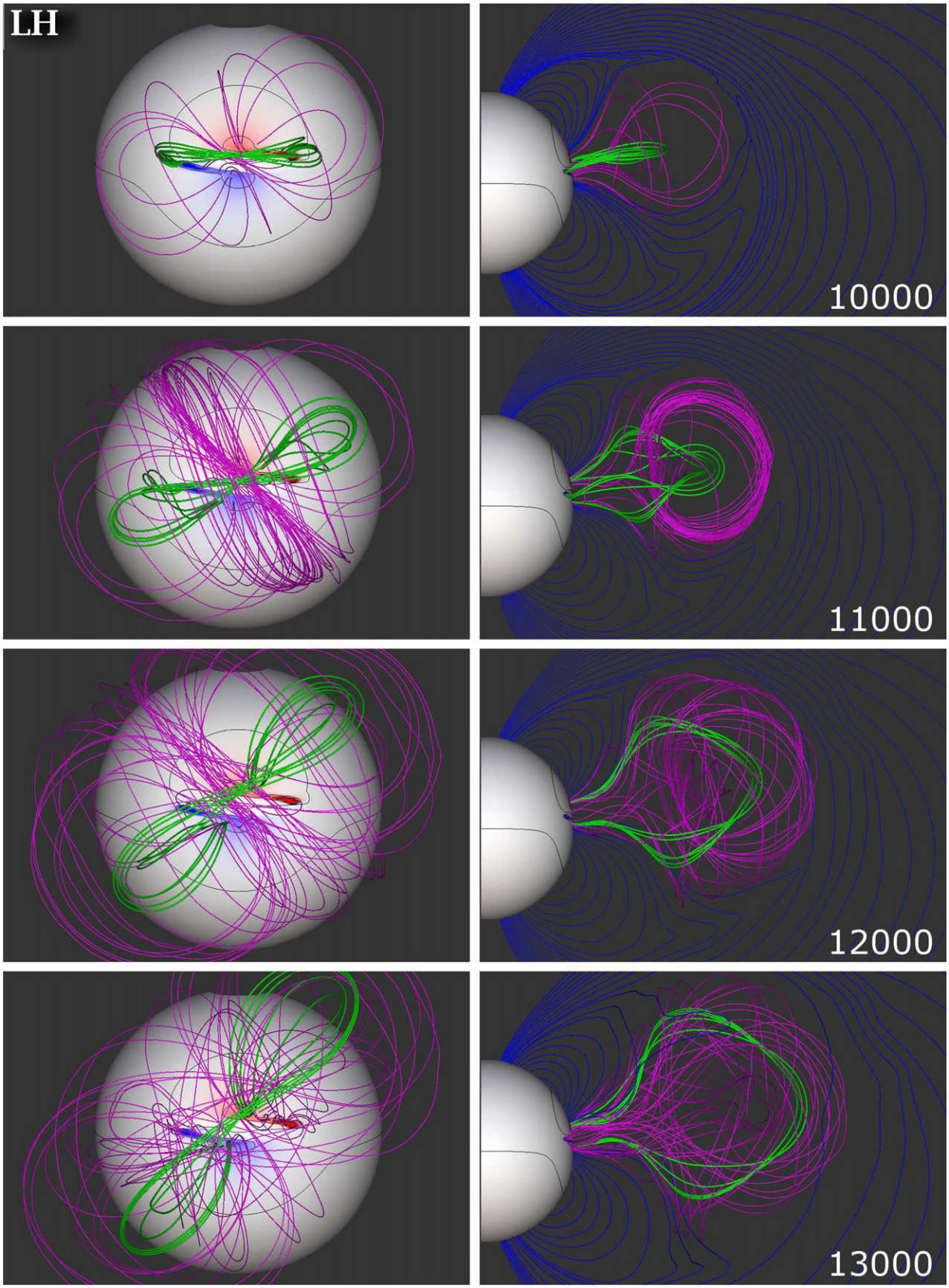

Figure 3. Temporal evolution of the erupting field structure for the LH simulation from a face-on (left column) and side-view (right column) perspectives. The green and magenta field lines represent the orientation of the axial (toroidal) and azimuthal (poloidal) flux during the eruption. The counterclockwise rotation of the LH flux rope structure is clear. See the text for additional details.

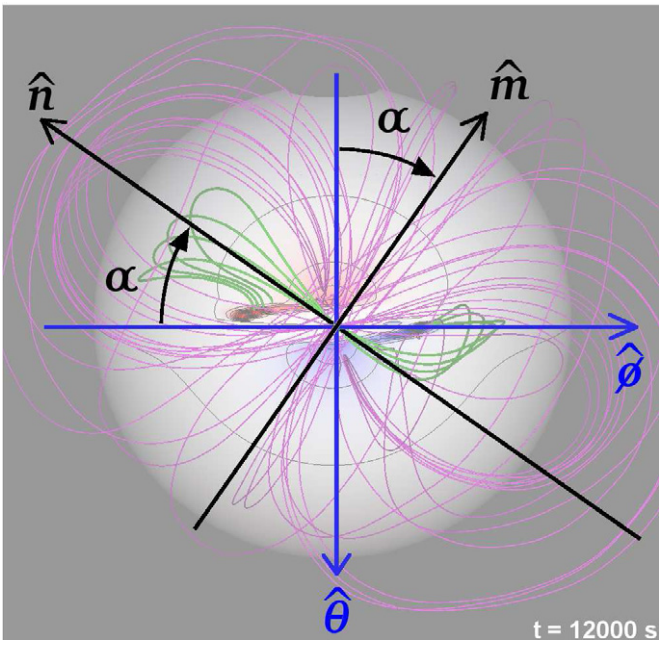

Figure 4. Illustrative example of the method used to determine the average rotation angle α from the face-on view of the axial/toroidal (green) and boundary/poloidal (magenta) field lines for a time slice of the RH simulation at $t = 12{,}000$ s.

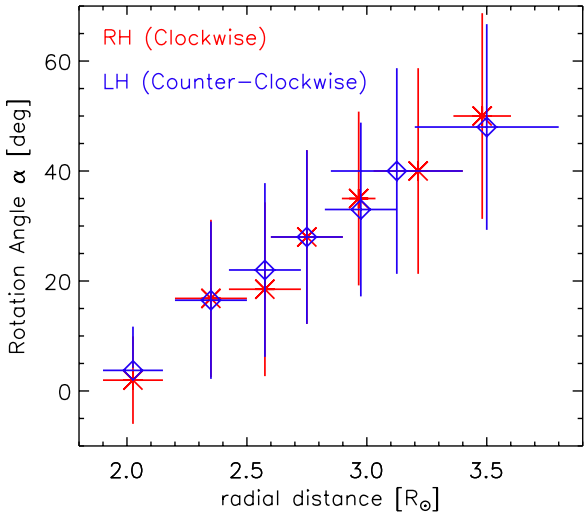

Figure 5. Radial evolution of the magnitude of the angle between the axes of the RH (red, clockwise) and LH (blue, counterclockwise) erupting flux rope structures and the respective active-region neutral lines. The X- and Y-axis error bars represent the range in radial distance of the traced axial field lines and the spread in angle of those field lines for each time slice, respectively.

the bulk flow velocities. Figure 6 shows two isosurfaces of $v_\theta = \pm 200$ km s^{-1}, for the LH and RH simulations (shown in the left and right columns, respectively) at $t = 11{,}000$ s. The red and purple arrows are to remind the reader that the positive (negative) $\hat{\boldsymbol{\theta}}$ direction points toward the southern (northern) poles. The signature of the rotation is clearly visible in the isosurface plots with approximately each half of the flux rope moving in opposite directions.

The physical origin for the observed rotation in our simulation is straightforward. Ultimately, it is due to the evolution of the Lorentz force $\boldsymbol{j} \times \boldsymbol{B}$ during the initial expansion of the sheared core field. Let us consider the forces acing on this field prior to eruption. Figure 2 shows the sigmoidal structure of the highly stressed field before the onset of the eruptive flare reconnection. The S- and inverse-S shapes of the RH and LH configurations are clearly visible. Note that this sigmoidal shape is a generic feature of the sheared-arcade model (Antiochos et al. 1994), and is essential for reconciling the model with prominence observations which typically show that prominences have inverse polarity (Bommier 1998). At the "elbows" of the sigmoids, there must be a magnetic tension force acting so as to straighten out the sigmoids. This tension force is balanced, however, by a magnetic pressure force due to the variation of flux density at the photosphere. It can be seen in Figure 2 that as a result of the shear, the flux distribution has become highly skewed so that strong flux is directly across the PIL from weak flux.

As long as the sheared core field is held down near the photosphere by the overlying unsheared flux, the magnetic tension and pressure forces in the sheared field core are in equilibrium. The external magnetic tension associated with the overlying restraining field and its removal is an integral element of the eruption process (Klimchuk 2001). In our simulations, magnetic breakout reconnection is the physical mechanism by which the quasi-equilibrium balance between the highly sheared low-lying flux and the unsheared overlying flux is disrupted. As the sheared field core rises and expands during the eruption, both the external tension (restraining) forces from the unsheared background field and the internal magnetic pressure in the sheared field core decrease. The eruption-induced decrease of the two components opposing the internal sigmoidal tension forces causes the entire core field to rotate in response to the imbalance. In principle, the rotation should stop once the core field straightens out, but as is evident from Figure 5, the rotation sets in early in the eruption and stays approximately constant throughout the simulation. Consequently, the core field appears to overshoot its equilibrium position and adopt a sigmoidal shape opposite to the initial sigmoid. The reason is that as the field lines stretch outward, the magnitude of the internal magnetic tension force decreases rapidly so that the angular momentum imparted in the early phase of the eruption maintains the rotation.

An interesting prediction from our results is that the amount and rate of rotation observed in an eruption should be proportional to the degree of "sigmoidality." A very pronounced sigmoid shape should lead to a rapid rotation of the filament field. Conversely, it is possible to obtain an eruption with little or no rotation, if the pre-eruption core field appears to be straight. Thus, while newly emerged active regions have flux distributions that are much more compact than our final sheared state, we argue that the amount of rotation ought to be determined by the coronal structure of the associated sheared field core. If a newly emerged active region, regardless of size, has a soft X-ray sigmoid skew similar to our MHD simulation fields, then we would expect a similar 40°–50°rotation during its eruption. A related prediction is that amount of rotation observed in an eruption is not directly related to the amount of helicity of the pre-eruption field. Note that the bulk of the helicity in our pre-eruption field is in the linkage between the sheared core field and the overlying unsheared field. Only a negligible fraction of the total helicity is due to the small twist inherent to the differentially sheared core field. Therefore, even if the core field had no sigmoidal shape, it would have essentially the same helicity, as one with a pronounced sigmoidal shape, but we claim that the latter would not rotate. This is, in fact, exactly what is seen in the equatorially symmetric three-dimensional breakout

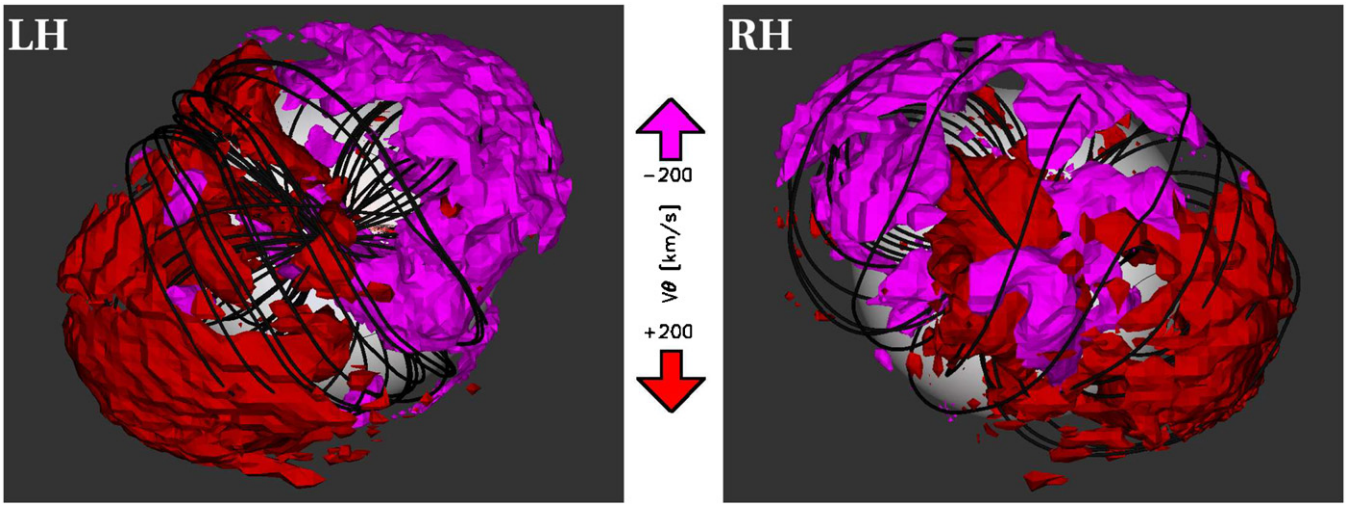

Figure 6. Left (right) panels plot isosurfaces of the θ-component of the plasma velocity in the LH (RH) simulations at time $t = 11{,}000$ sec. The red and magenta isosurfaces are at ± 200 km s^{-1} respectively and the arrows indicate the positive (negative) directions of $\hat{\boldsymbol{\theta}}$, pointing toward the Southern (Northern) poles. The overall torque leading to the large scale rotation of the flux rope structures is clearly evident and in the opposite direction for the two cases.

simulations by DeVore & Antiochos (2008). There, the erupting sheared fields do not exhibit any large-scale rotational dynamics, due primarily to their more balanced flux distribution which gives rise to a strong shear component with very little sigmoidal shape despite having similar sheared field footpoint separation.

3.2. Flare-Induced Rotation

Note that in the above discussion of the rotation, no mention was made of the possibility of a kink like instability. The reason is that the pre-eruption sheared field has very little twist, at most half a turn due to the differential shear. Since the rotation that we observe sets in almost immediately during the eruption, it cannot be due to a kink. Also, the field does not appear to deform toward a helical shape; it merely rotates out of its sigmoidal shape.

Although there is essentially no twist prior to eruption, the flare reconnection during eruption produces a twisted flux rope by converting the overlying unsheared field into a highly twisted sheath surrounding the erupting core field. This can be seen in the field line plots of Figure 3 and also in Figure 7 that plots B_ϕ on a semitransparent plane at $\phi = 0^\circ$ (panel (a)) and plots B_θ on the cone $\theta = 80.^\circ 15$ (panel (c)) along with representative ejecta field lines for the RH flux rope at $t = 11{,}000$ s. It is possible, therefore, that as the eruption proceeds, enough twist is built up in the erupting flux rope that it becomes kink unstable. In order to determine whether our erupting structure becomes susceptible to the kink instability, we have made a quantitative estimate of the relative axial (toroidal $\Phi_{\rm T}$) and twist (poloidal $\Phi_{\rm P}$) fluxes to compare to the typical critical twist limit threshold and the time evolution of these values.

The toroidal and poloidal fluxes are estimated from the simulation data as

$$\Phi_{\rm T} \sim \sum_i \boldsymbol{B}(\boldsymbol{r}_i) \cdot \Delta \boldsymbol{A}_{n,i}\ , \quad \Phi_{\rm P} \sim \sum_j \boldsymbol{B}(\boldsymbol{r}_j) \cdot \Delta \boldsymbol{A}_{m,j}, \qquad (3)$$

where the indicies i, j represent cells in the integration area of two-dimensional cuts through the simulation data corresponding to the m- and n-planes defined by their perpendicular unit vectors $(\hat{\boldsymbol{n}}, \hat{\boldsymbol{m}})$. The flux rope coordinate system is given by a simple rotation of the standard $(\hat{\boldsymbol{\theta}}, \hat{\boldsymbol{\phi}})$ unit vectors in spherical coordinates, defined by the average rotation angle α of the erupting flux rope structure with respect to the radial direction at $(\theta, \phi) = (80.^\circ 15, 0^\circ)$degrees (as shown in Figure 4). Likewise, the elemental area associated with a summation over the flux rope cross section $\Delta \boldsymbol{A}_n$ and lengthwise through the flux rope structure $\Delta \boldsymbol{A}_m$ are given by a similar projection of the θ-, ϕ-planar area elements in the time-varying local flux rope coordinate system, yielding

$$\Delta \boldsymbol{A}_{n,i} = -\sin\alpha (r_i \sin\theta_i \Delta\phi) \Delta r_i \hat{\boldsymbol{\theta}} - \cos\alpha (r_i \Delta\theta) \Delta r_i \hat{\boldsymbol{\phi}}, \qquad (4)$$

$$\Delta \boldsymbol{A}_{m,j} = -\cos\alpha (r_j \sin\theta_j \Delta\phi) \Delta r_j \hat{\boldsymbol{\theta}} + \sin\alpha (r_j \Delta\theta) \Delta r_j \hat{\boldsymbol{\phi}}. \qquad (5)$$

Note that the computational grid spacing is linear for both angles ($\Delta\theta = 0.98^\circ$, $\Delta\phi = 1.13^\circ$) whereas the radial grid spacing is logarithmic ($\Delta r_i / r_i = 0.0189$). Also, the quantitative flux calculation uses only the rebinned ARMS data in the finest resolution subregion of the computational domain, which contains the whole flux rope structure through $\sim$13,000 s.

The definition of the spatial extent of the flux rope ejecta, and therefore the limits of the $\boldsymbol{B} \cdot \Delta \boldsymbol{A}$ integration in any given time slice, is not trivial. Figures 7(b) and (d) show an example of the procedure used to estimate the integration boundaries for the RH simulation at $t = 11{,}000$ seconds. For each output time we have defined two-dimensional pixel masks in the r–n and r–m planes, indicated by the black contours. The pixel mask in the n-plane (upper plots) represents an integral from the flux rope axis to its boundary and along the entire flux rope length. We take $\boldsymbol{B} \cdot \hat{\boldsymbol{m}} \geqslant 0$ to represent one sign of the poloidal/azimuthal flux (defining the flux rope axis as $\boldsymbol{B} \cdot \hat{\boldsymbol{m}} = 0$) and a loop like inner flux rope boundary at $R_{\rm cs}$, where $R_{\rm cs}$ is the radial extent of the flare current sheet in the m-plane. The pixel mask in the m-plane (lower plots) represents an integral over the entire flux rope cross section for the calculation of the axial/toroidal flux. Here, we define the flux rope axial field as $\boldsymbol{B} \cdot \hat{\boldsymbol{n}} \leqslant 0$ in the RH case and $\geqslant 0$ in the LH case. Therefore, the maximum radial outer boundary for the integration contours in the n-plane should be, approximately, the flux rope axis, which should roughly correspond to the center of the integration region (flux rope cross section) in the m-plane. The integration pixel masks were checked by visual inspection against the three-dimensional rendering of the corresponding field components on constant ϕ, θ surfaces and the highly twisted field lines representing the ejecta boundary.

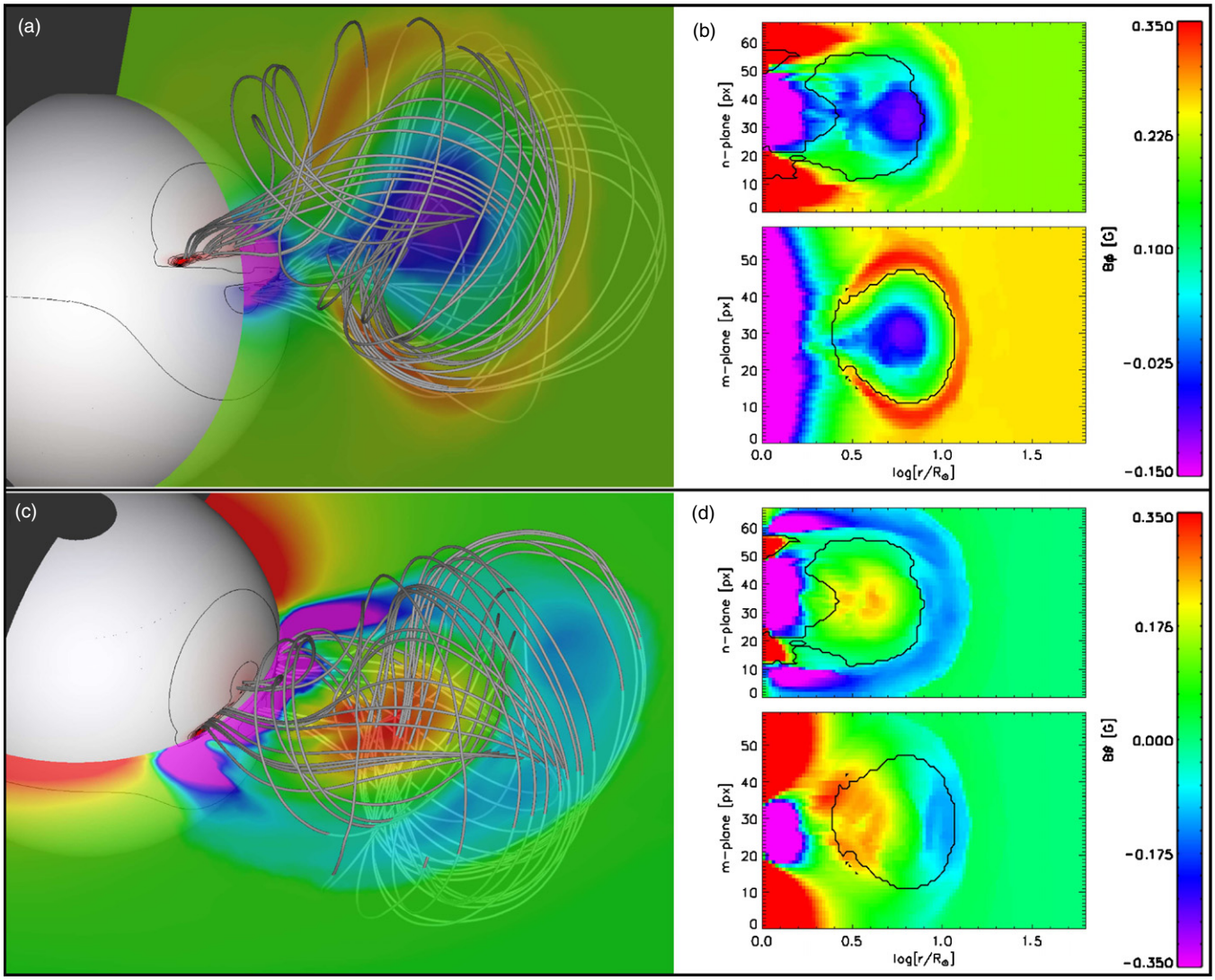

Figure 7. Example of the procedure to estimate the ejecta fluxes in simulation data at time $t = 11{,}000$ seconds. Panel (a) shows B_ϕ as a transparent coordinate slice at $\phi = 0^\circ$ alongside representative field lines showing the flux rope structure. Panel (b) plots two-dimensional cuts of B_ϕ in the r–n (top) and r–m plane (bottom). The black contours represent the integration boundaries used to estimate the CME axial and azimuthal/twist fluxes discussed in Section 3.2. Panels (c) and (d) are in the same format, showing B_θ as a transparent coordinate slice on the cone $\theta = 80.^\circ 15$ with the same representative flux rope field lines, and B_θ in the r–n and r–m planes with the contours showing the flux integration boundaries.

To link the coordinate systems to previous observational work, the rotation angle α is also known as the clockangle (e.g., Yurchyshyn 2008; Kilpua et al. 2009), the direction of $\hat{\boldsymbol{n}}$ is along the ellipse major axis and would be the axis of symmetry in in situ flux rope modeling or reconstruction (Lepping et al. 1990; Hu & Sonnerup 2001) and $\hat{\boldsymbol{m}}$ points along the ellipse minor axis and lies in the plane perpendicular to the in situ flux rope axis. It is also worth noting that there appears a well-defined region of compressed field surrounding the flux rope ejecta with a B_ϕ component opposite that of the internal flux rope fields. This compressed field is in the sheath between the leading expansion wave and the flux rope driver. Enhanced and compressed fields in ICME sheath regions are a common occurrance (Tsurutani et al. 1988; Zhang et al. 2004).

Figure 8 plots the temporal evolution of the toroidal and poloidal flux magnitudes for several times during the flux rope eruption with the RH simulation results shown in red and the LH simulation results shown in blue. In both cases, the axial (toroidal) flux Φ_T, shown as solid lines (and RH/LH symbols as Xs/diamonds), remains approximately constant, as expected, because it represents the imposed shear component of the pre-eruptive structure. The quantitative value of both the RH and LH Φ_T magnitude of $\sim 10^{21}$ Mx is well within the broad range of observed in situ MC toroidial fluxes (e.g., Lynch et al. 2005). The poloidal flux Φ_P, shown as dotted lines with RH/LH symbols as squares/triangles, represents the initially unsheared overlying flux of the pre-eruptive structure that is converted into the twist component of the ejecta during the eruptive flare reconnection. The arrow placed at 10,000 s indicates the approximate onset of the eruptive flare reconnection with the first visible time dump showing reconnected, twisted field lines and represents the beginning of the average rotation angle measurements of Figure 5. Φ_P is seen to increase rapidly for approximately 20 minutes during the initial impulsive phases of the flare before gradually leveling off to an approximately constant value. The quantitative differences (of roughly a factor 2) between the RH and LH poloidal fluxes shows the estimation error associated with the integration pixel masks. We expect both Φ_T and Φ_P to decrease during continued propagation which can be explained by some amount of ejecta flux being continually removed via

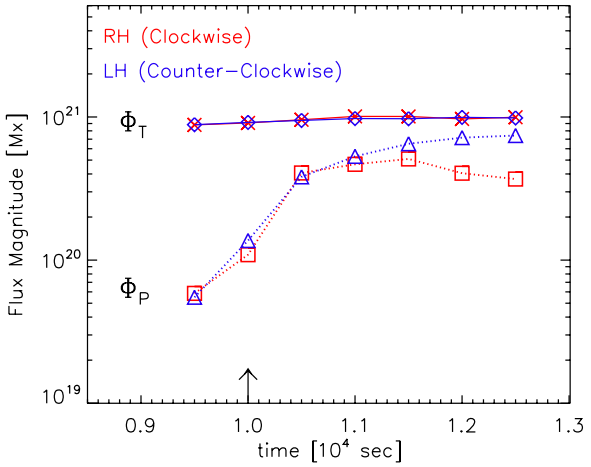

Figure 8. Temporal evolution of the toroidal (Φ_T, solid lines) and poloidal (Φ_P, dashed lines) fluxes associated with the erupting flux rope structures created during the flare reconnection for the RH (red) and LH (blue) simulations. The arrow at $t = 10{,}000$ seconds shows the first data point used in the average angle measurements in Figure 4. While Φ_T agrees well in the LH and RH cases, Φ_P shows a slight divergence toward the latter part of the simulations, indicating the relative error associated with our integration pixel masks. The ratio of these fluxes $q = 2\Phi_T/\Phi_P > 2$ is used to show our breakout eruption flux ropes are not becoming unstable to the first external kink mode ($q \lesssim 1$).

the overlying breakout reconnection that proceeds throughout the simulation and some amount passing through the boundaries of the fine-grid region due to the rapid expansion of the erupting structure.

The critical twist threshold for the kink instability of a flux rope structure is typically given as $>2.5\pi$ over the length of the flux rope (e.g., Hood & Priest 1979; Török & Kliem 2003), with the exact value depending on the relevant parameters associated with the geometry of the flux rope and the background field strengths (Linton et al. 1996). This threshold can also be expressed in terms of the so-called safety factor, the ratio of toroidal (axial) to poloidal (twist) flux, for a cylindrical pinch $q \sim 2\Phi_T/\Phi_P$ (e.g., Bateman 1978). The kink mode can be thought of as the tendency of a straight twisted flux rope to increase its length by writhing so that the axis becomes helical and, thereby, decreases the energy in the twist component of the field if this component becomes sufficiently large. In terms of our flux ratio criterion, a simple cylindrical rope goes kink unstable if $q \lesssim 1$ (Bateman 1978). It is clear from Figure 8 that our stability values are always $q \gtrsim 2$. Therefore, we conclude that the kink instability is not responsible for the rotation observed in our simulation and is unlikely to play any role in the evolution of the eruption, at least, to the end of the simulation. Of course, if the twist flux continues to build as a result of flare reconnection, a kink may well occur.

4. CONCLUSIONS

We have shown that, in sheared arcade magnetic breakout eruptions, the resulting flux ropes *created by the flare reconnection* undergo significant rotation during their propagation through approximately 2 $R_\odot$ of the closed field corona. Therefore, observations of filament rotation and/or axial writhe occurring *during* or *after* the onset of flare reconnection are not sufficient to prove that the pre-eruption magnetic field configuration was that of a twisted flux rope in the corona.

From our simulations, we predict that the magnitude of rotation is related to the degree of "sigmoidality" of the pre-eruption field configuration, i.e., just how skewed is the sheared field structure that overlies the PIL. The rotational signature of kink-unstable flux rope CMEs may be quite different than our sheared arcade breakout results, although the direction of rotation has the same chirality dependence. We have argued that our simulations of breakout CME eruptions can be considered representative of essentially all of the standard sheared-arcade CME models, in particular, we expect flux-cancellation and tether-cutting initiated flux ropes to behave quite similarly during the initial phases of the eruption. The eruptive flare plays the same role in all three scenarios, converting originally sheared fields into flux rope CME structures while facilitating the eruption process. There is one important difference between the breakout model sheared arcade eruption and a tether-cutting or flux cancellation eruption occurring in a globally bipolar field. The overlying breakout reconnection arises due to the topology of the multipolar field configuration and is present throughout the entire eruption process. This breakout reconnection acts to remove ejecta flux during CME transit through the closed field corona. CMEs originating in globally bipolar fields do not have an analogous twist flux removal mechanism, so it may be the case that bipolar sheared arcade eruptions are able to reach the kink-instability poloidal flux threshold more easily than multipolar eruptions.

Clearly, more quantitative studies of CME rotation are needed in order to determine, if possible, which observable physical properties of the source region best correlate with the amount of rotation estimated for CME and ICME/MC event pairs. For example, an observational study focusing on the pre-eruption sigmoid skew and the differences in the source region PIL, the resulting halo CME geometry, and the in situ MC orientation for well observed sigmoid-CME-MC events could test our hypothesized skew–rotation relationship. Likewise, a measure of the CME source region flux distribution separation may reveal a statistically significant dependence on the footpoint separation in the erupting flux rope configuration. Both of these possibilities could be, and should be, tested through numerical modeling as well.

The fact that our breakout-initiated eruption (and by proxy sheared-field CMEs in general) and kink-unstable flux rope CMEs may be susceptible to similar rotational dynamics, at least direction wise, would support the idea that this type of large scale rotation could be a universal feature of CME eruptions. If the magnitude of rotation seen in our simulations was similar to the rotation predicted from kink-unstable flux rope simulations, then the Yurchyshyn (2008) $\pm 45^\circ$ "disagreement" typically associated with the evolution of CME magnetic orientation may be unavoidable. While this represents an additional obstacle to the already challenging task of forecasting the B_z-component of ICME transients, it should be possible to incorporate the predicted rotation effects of various CME models with pre-eruption observations of source region magnetic field orientation.

However, the rapid expansion associated with the eruption means there is a rapid transformation in the ejecta spatial scale, potentially from active region size scales, to whole-Sun scales, and eventually to heliospheric scales. Consequently, it may be that the relatively straightforward (and predictable) rotation effects seen here in the low corona are completely washed out or dominated by the larger scale streamer-belt orientation and/or coronal hole structure, or eventually by the solar wind stream and heliospheric magnetic sector structure. Ultimately, we will need full Sun-to-Earth numerical modeling that captures both the dynamics of the eruption close to the Sun and the ICME

propagation through the heliosphere in order to understand all these fundamental interactions between CMEs and their interplanetary environment.

B.J.L. gratefully acknowledges grants NSF SHINE ATM-0621725 and NASA HGI NNX08AJ04G. Additional support for this work comes from the NASA HTP and SR&T Programs, the Office of Naval Research (ONR), and SSL/UCB participation in the Center for Integrated Space-Weather Modeling (CISM) Collaboration. The DoD High Performance Computing Modernization Program provided resources at the ERDC major shared resource and NRL-DC distributed computing centers for this research.

REFERENCES

Antiochos, S. K., Dahlburg, R. B., & Klimchuk, J. A. 1994, ApJ, 420, L41
Antiochos, S. K., DeVore, C. R., & Klimchuk, J. A. 1999, ApJ, 510, 485
Bateman, G. 1978, MHD Instabilities (Cambridge: MIT Press)
Bommier, V. 1998, in ASP Conf. Ser. 150, New Perspectives on Solar Prominences, ed. D. Webb, D. Rust, & B. Schmieder (San Francisco, CA: ASP), 434
Borrini, G., Gosling, J. T., Bame, S. J., & Feldman, W. C. 1982, J. Geophys. Res., 87, 7370
Bothmer, V., & Schwenn, R. 1998, Ann. Geophys., 16, 1
Burlaga, L. F. 1988, J. Geophys. Res., 93, A7, 7217
Cane, H. V., Richardson, I. G., & Wibberenz, G. 1997, J. Geophys. Res., 102, 7075
Canfield, R. C., Hudson, H. S., & McKenzie, D. E. 1999, Geophys. Res. Lett., 26, 6, 627
Canfield, R. C., Kazachenko, M. D., Acton, L. W., Mackay, D. H., Son, J., & Freeman, T. L. 2007, ApJ, 671, L81
Chae, J., Wang, H., Qiu, J., Goode, P. R., & Wilhelm, K. 2000, ApJ, 533, 535
Cremades, H., & Bothmer, V. 2004, A&A, 422, 307
Crooker, N. U., Siscoe, G. L., Shodhan, D., Webb, D. F., Gosling, J. T., & Smith, E. J. 1993, J. Geophys. Res., 98, 9371
Dere, K. P., Brueckner, G. E., Howard, R. A., Michels, D. J., & Delaboudiniere, J. P. 1999, ApJ, 516, 465
DeVore, C. R. 1991, J. Comput. Phys., 92, 142
DeVore, C. R., & Antiochos, S. K. 2008, ApJ, 680, 740
Fan, Y., & Gibson, S. E. 2004, ApJ, 609, 1123
Galvin, A. B. 1997, in Coronal Mass Ejections, Geophys. Monogr. Ser. 99, ed. N. Crooker, J. A. Joselyn, & J. Feynman (Washington, DC: AGU), 253
Goldstein, H. 1983, in Solar Wind Five, NASA Conf. Publ. CP-2280, ed. M. Neugebauer (Washington, DC: NASA), 731
Gosling, J. T. 1990, in Physics of Magnetic Flux Ropes, Geophys. Monogr. Ser. 58, ed. C. T. Russel, E. R. Priest, & L. C. Lee (Washington, DC: AGU), 9
Green, L. M., Kliem, B., Török, T., van Driel-Gesztelyi, L., & Attrill, G. D. R. 2007, Sol Phys., 246, 365
Gosling, J. T., Baker, D. N., Bame, S. J., Feldman, W. C., Zwickl, R. D., & Smith, E. J. 1987, J. Geophys. Res., 92, 8519
Gosling, J. T., Pizzo, V., & Bame, S. J. 1973, J. Geophys. Res., 78, 2001
Hildago, M. A., Cid, C., Medina, J., & Viñas, A. F. 2002, J. Geophys. Res., 107, A1, 1002
Hood, A. W., & Priest, E. R. 1979, Sol Phys., 64, 303
Hu, Q., & Sonnerup, B. U. Ö. 2001, Geophys. Res. Lett., 28, 467
Hundhausen, A. J. 1999, in The Many Faces of the Sun: A Summary of the Results from NASA's Solar Maximum Mission, ed. K. T. Strong, J. L. R. Saba, B. M. Haisch, & J. T. Schmelz (New York: Springer), 143
Huttunen, K. E. J., Schwenn, R., Bothmer, V., & Koskinen, H. E. J. 2005, Ann. Geophys., 23, 625
Illing, R. M. E., & Hundhausen, A. J. 1986, J. Geophys. Res., 91, 10951
Kilpua, E. K. J., et al. 2009, Solar Phys., 254, 325
Klein, L. W., & Burlaga, L. F. 1982, J. Geophys. Res., 87, 613
Klimchuk, J. A. 2001, in Space Weather, Geophys. Monogr. Ser. 125, ed. P. Song, H. J. Singer, & G. L. Siscoe (Washington, DC: AGU), 143
Krall, J., Yurchyshyn, V. B., Slinker, S., Skoug, R. M., & Chen, J. 2006, ApJ, 642, 541
Lepping, R. P., Burlaga, L. F., & Jones, J. A. 1990, J. Geophys. Res., 95, A8, 11957
Li, Y., Luhmann, J. G., Fisher, G. H., & Welsch, B. T. 2004, J. Atmos. Sol.-Terr. Phys., 66, 1271
Lin, Y., Martin, S. F., & Engvold, O. 2008, in ASP Conf. Ser. 383, Subsurface and Atmospheric Influences on Solar Activity, ed. R. Howe, R. W. Komm, K. S. Balasubramaniam, & G. J. D. Petrie (San Francisco, CA: ASP), 243
Linton, M. G., Longcope, D. W., & Fisher, G. H. 1996, ApJ, 469, 954
Lynch, B. J., Antiochos, S. K., DeVore, C. R., Luhmann, J. G., & Zurbuchen, T. H. 2008, ApJ, 683, 1192
Lynch, B. J., Gruesbeck, J. R., Zurbuchen, T. H., & Antiochos, S. K. 2005, J. Geophys. Res., 110, A08107
MacNeice, P. J., Antiochos, S. K., Phillips, A., Spicer, D. S., DeVore, C. R., & Olson, K. M. 2004, ApJ, 614, 1028
MacNeice, P. J., Olson, K. M., Mobarry, C., de Fainchtein, R., & Packer, C. 2000, Comput. Phys. Commun., 126, 330
Magara, T., & Longcope, D. W. 2003, ApJ, 586, 630
Manchester, W. B., IV. 2001, ApJ, 547, 503
Manchester, W. B., IV. 2003, J. Geophys. Res., 108, A4, 1162
Manchester, W. B., IV 2008, in ASP Conf. Ser. 383, Subsurface and Atmospheric Influences on Solar Activity, ed. R. Howe, R. W. Komm, K. S. Balasubramaniam, & G. J. D. Petrie (San Francisco, CA: ASP), 91
Marabushi, K. 1986, Adv. Space Res., 6, 6, 335
Martin, S. F. 1998, Sol. Phys., 182, 107
Moore, R. L., Sterling, A. C., Hudson, H., & Lemen, J. R. 2001, ApJ, 552, 833
Mulligan, T., & Russell, C. T. 2001, J. Geophys. Res., 106, A6, 10581
Mulligan, T., Russell, C. T., & Luhmann, J. G. 1998, Geophys. Res. Lett., 25, 15, 2959
Panasenco, O., & Martin, S. F. 2008, in ASP Conf. Ser. 383, Subsurface and Atmospheric Influences on Solar Activity, ed. R. Howe, R. W. Komm, K. S. Balasubramaniam, & G. J. D. Petrie (San Francisco, CA: ASP), 243
Pevtsov, A. A., Canfield, R. C., & Metcalf, T. R. 1995, ApJ, 440, L109
Plunkett, S. P., et al. 2000, Sol. Phys., 194, 371
Richardson, I. G., & Cane, H. V. 1995, J. Geophys. Res., 100, 23397
Rust, D. M., & Kumar, A. 1996, ApJ, 464, L199
Sheeley, N. R., Jr. 2005, Living Rev. Solar Phys., 2, 5, URL: http://www.livingreviews.org/lsrp-2005-5 (cited on 23 Nov 2008)
Strous, L. H., Scharmer, G., Tarbell, T. D., Title, A. M., & Zwaan, C. 1996, A&A, 306, 947
Thernisien, A. F. R., Howard, R. A., & Vourlidas, A. 2006, ApJ, 652, 763
Török, T., & Kliem, B. 2003, A&A, 406, 1043
Török, T., Kliem, B., & Titov, V. S. 2004, A&A, 413, L27
Tsurutani, B. T., Gonzalez, W. D., Tang, F., Akasofu, S. I., & Smith, E. J. 1988, J. Geophys. Res., 98, A8, 8519
van Ballegooijen, A. A., Cartledge, N. P., & Priest, E. R. 1998, ApJ, 501, 866
Vandas, M., Fischer, S., Pelant, P., & Geranios, A. 1993, J. Geophys. Res., 98, A7, 11467
Yurchyshyn, V. 2008, ApJ, 675, L49
Yurchyshyn, V., Hu, Q., Lepping, R. P., Lynch, B. J., & Krall, J. 2007, Adv. Space Res., 40, 1821
Yurchyshyn, V., Wang, H., Goode, P. R., & Deng, Y. 2001, ApJ, 563, 381
Zhang, J., Liemohn, M. W., Kozyra, J. U., Lynch, B. J., & Zurbuchen, T. H. 2004, J. Geophys. Res., 109, A9, A09101
Zhao, X. P., & Hoeksema, J. T. 1996, J. Geophys. Res., 101, A3, 4825
Zhao, X. P., & Hoeksema, J. T. 1998, J. Geophys. Res., 103, A2, 2077
Zurbuchen, T. H., & Richardson, I. G. 2006, Space Sci. Rev., 123, 31
Zwickl, R. D., Asbridge, J. R., Bame, S. J., Feldman, W. C., Gosling, J. T., & Smith, E. J. 1983, in Solar Wind Five, NASA Conf. Publ. CP-2280, ed. M. Neugebauer (Washington, DC: NASA), 711